Real-Time Profiling of Fine-Grained Air Quality Index Distribution Using UAV Sensing

Yuzhe Yang, *Student Member, IEEE*, Zijie Zheng, *Student Member, IEEE*, Kaigui Bian, *Member, IEEE*, Lingyang Song , *Senior Member, IEEE*, and Zhu Han, *Fellow, IEEE*

Abstract—Given significant air pollution problems, air quality index (AQI) monitoring has recently received increasing attention. In this paper, we design a mobile AQI monitoring system boarded on the unmanned-aerial-vehicles, called *ARMS*, to efficiently build fine-grained AQI maps in real-time. Specifically, we first propose the Gaussian plume model on the basis of the neural network (GPM-NN), to physically characterize the particle dispersion in the air. Based on GPM-NN, we propose a battery efficient and adaptive monitoring algorithm to monitor AQI at the selected locations and construct an accurate AQI map with the sensed data. The proposed adaptive monitoring algorithm is evaluated in two typical scenarios, a 2-D open space like a roadside park, and a 3-D space like a courtyard inside a building. The experimental results demonstrate that our system can provide higher prediction accuracy of AQI with GPM-NN than other existing models, while greatly reducing the power consumption with the adaptive monitoring algorithm.

Index Terms—Air quality, fine-grained monitoring, mobile sensing, unmanned aerial vehicle (UAV).

I. Introduction

IN A recent report from the World Health Organization [1], air pollution has become the world's largest environmental health risk, as one in eight of global deaths are caused by the air pollution exposure each year. Air pollution is caused by gaseous pollutants that are harmful to humans and ecosystem, especially concentrated in the urban areas of developing countries. Thus, reducing air pollution would save millions of lives, and many countries have invested significant efforts on monitoring and reducing the emission of air pollutants. Government agencies have defined air quality index (AQI) to quantify the degree of air pollution. AQI is calculated based on the concentration of a number of air pollutants (e.g., the concentration

Y. Yang, Z. Zheng, K. Bian, and L. Song are with the School of Electrical Engineering and Computer Science, Peking University, Beijing 100871, China (e-mail: yuzhe.yang@pku.edu.cn; zijie.zheng@pku.edu.cn; bkg@pku.edu.cn; lingyang.song@pku.edu.cn).

Z. Han is with the Electrical and Computer Engineering Department and the Computer Science Department, University of Houston, Houston, TX 77004 USA, and also with the Department of Computer Science and Engineering, Kyung Hee University, Seoul, South Korea (e-mail: zhan2@uh.edu).

of $PM_{2.5}$, PM_{10} particles, and so on in developing countries). A higher value of AQI indicates that air quality is "heavily" or "seriously" polluted, resulting in a greater proportion of the population may experience harmful health effects [2]. To intuitively reflect AQI value of locations in either 2-D or 3-D area, AQI map is defined to offer such convenience [3].

A. Mobile AQI Monitoring

AQI monitoring can be completed by sensors at the governmental static observation stations, generating an AQI map in a local area (e.g., a city [4]). However, these static sensors only obtain a limited number of measurement samples in the observation area and may often induce high costs. For example, there are only 28 monitoring stations in Beijing. The distance between two nearby stations is typically several 10 000 m, and the AQI is monitored every 2 h [5]. To provide more flexible monitoring and reduce the cost, mobile devices, such as cell phones, cars, and balloons are used to carry sensors and process real-time measuring. Crowd-sourced photographs contributed by the mass of cell phones can help depict the 2-D AQI map in a large geographical region in Beijing [6], with a range of 4 × 4 km. Mobile nodes equipped with sensors can provide 100 × 100 m 2-D on-ground concentration maps with relatively high resolution [7]–[9]. Sensors carried by tethered balloons can build the height profile of AQI at a fixed observation height within 1000 m [10]. A mobile system with sensors equipped in cars and drones can help monitor $PM_{2.5}$ in open 3-D space [11], with 200-m per measurement.

B. Motivations for Real-Time Fine-Grained Monitoring

Even though current mobile sensing approaches can provide relatively accurate and real-time AQI monitoring data, they are spatially coarse-grained, since two measurements are separated by few hundreds of meters in horizontal or vertical directions in the 3-D space. However, AQI has intrinsic changes from meters to meters, and it is preferred to perform AQI monitoring in the 3-D space surrounding an office building or throughout a university campus, rather than city-wide [12], [13]. The AQI distribution in meter-sliced areas, called as fine-grained areas would be desirable for people, particularly those living in urban areas. The fine-grained AQI map can help design the ventilation system for buildings, which for example can guide teachers and students to stay away from the pollution sources on campus [14].
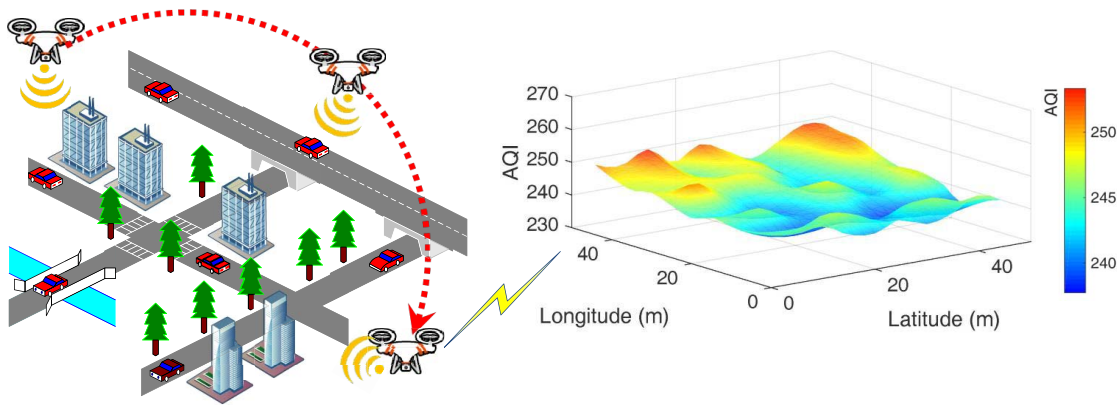
Fig. 1. Illustration of AQI measurement using mobile sensing over UAV.

Due to the high power consumption of mobile devices, one can only measure a limited number of locations of the entire space. To avoid an exhaustive measurement, using an estimation model to approximate the value of unmeasured area has been wildly adopted. In [15], the prediction model is based on a few public air quality stations and meteorological data, taxi trajectories, road networks, and point of interests. However, because they estimate AQI using a feature set based on historical data, their model cannot respond in real-time to the change in pollution concentration at an hourly granularity, leading to large errors at times. In [11], the random walk model is used for prediction by dividing the whole space into different shapes of cubes. However, the model may not reflect physical dispersion of particles [16], [17], and all locations are measured without considering the battery life constraint when mobile devices are used. Mobile sensor nodes used in [7] employ the regression model as well as graph theory to estimate the AQI value at unmeasured locations. However, they mainly focus on 2-D area, and can hardly produce a 3-D fine-grained map. Neural networks (NNs) are also used for forecasting on the AQI distribution [18]–[21]. However, its performance in fine-gained area is not satisfied without considering the physical characteristic of real AQI distribution.

C. Contributions

In this paper, we design a mobile sensing system based on unmanned-aerial-vehicles (UAVs), called *ARMS*, that can effectively catch AQI variance at meter-level and profile the corresponding fine-grained distribution. ARMS is a real-time monitoring system that can generate current AQI map within a few minutes, compared to the previous methods with an interval of a few hours. With ARMS, the fine-grained AQI map construction can be decomposed into two parts. First, we propose a novel AQI distribution model, named Gaussian plume model embedding NNs (GPM-NNs), that combines physical dispersion and nonlinear NN structure, to do predictions of unmeasured area. Second, we detail the adaptive monitoring algorithm as well as addressing its applications in a few typical scenarios. By measuring only selected locations in different scenarios, GPM-NN is used to estimate AQI value at unmeasured locations and generate real-time AQI maps, which can

save the battery life of mobile devices while maintaining high accuracy in AQI estimation.

The contributions of this paper are summarized as follows.
1) The GPM-NN is highly adaptive in different fine-grained measurement scenarios, and it can provide higher accuracy in creating AQI maps than other existing models.
2) The adaptive monitoring algorithm can guide UAV to choose optimized trajectory in different scenarios based on GPM-NN. It can greatly reduce the battery consumption of ARMS, while achieving high accuracy when constructing real-time AQI maps.
3) The ARMS is the first UAV sensing system for fine-grained AQI monitoring.

The rest of this paper is organized as follows. In Section II, we briefly introduce our UAV sensing system. In Section III, we present our fine-grained AQI distribution model. The adaptive monitoring algorithm is addressed in Section IV. In Sections V and VI, we present two typical application scenarios and performance analysis of ARMS, respectively. Finally, the conclusions are drawn in Section VII.

II. PRELIMINARIES OF UAV SENSING SYSTEM

In this section, first we provide a brief introduction of ARMS, and then we show how to construct a dataset using ARMS. To confirm the reliability of the collected dataset, we compare the collected data and the official AQI measured by the nearest Beijing government's monitoring station, i.e., the Haidian station [22]. To determine the parameters of our model, we test possible factors that may influence AQI, such as wind, locations, etc., and remove those factors that have small correlations with AQI in the fine-grained scenarios from our model.

A. System Overview

The architecture of ARMS includes an UAV and an air quality sensor boarded on the UAV, as shown in Fig. 2. The sensor is fixed in a plastic box with vent holes, bundled on the bottom of UAV. The sensor uses a laser-based AQI detector [23], which can provide the concentration within $\leq \pm 3\%$ monitor error for common pollutants in AQI calculation, such as
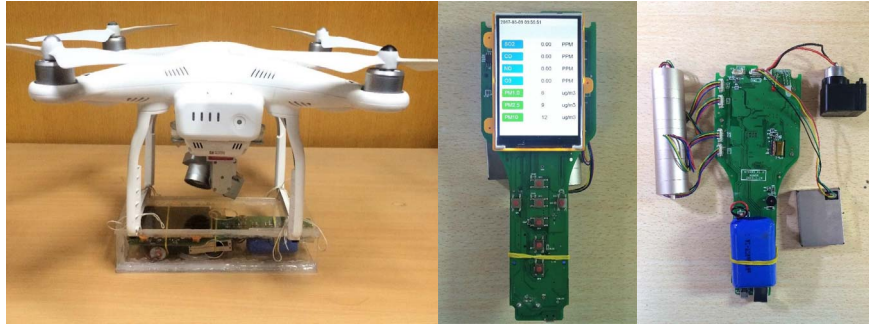
Fig. 2.   ARMS system, the front and the back of the sensor board.

$PM_{2.5}$, PM_{10}, CO, NO, SO_2, and O_3. The values of these pollutants are real-time recorded, with which we calculate the corresponding AQI value at measuring locations.

For the UAV, we select DJI Phantom 3 Quadcopter [24] as the mobile sensing device. The UAV can keep hosting for at most 15 min due to the battery constraint, which restricts the longest continuous duration within one measurement. The GPS sensor on the UAV can provide the real-time 3-D position. During one measurement, the UAV is programmed with a trajectory, including all locations that need to be measured. Following this trajectory, UAV hovers for 10 s to collect sufficient data to derive the AQI value at each stop, before moving to the next one.

During one monitoring process, ARMS measures all target locations and records the corresponding AQI values. After the measuring process is completed, the data is then sent to the offline PC and put into the GPM-NN model to construct the real-time AQI map. Thus, the map construction process is offline.

B. Dataset Description

Data collected by ARMS are then arranged as a dataset.[1] As shown in Fig. 1, we have conducted a measurement study in both typical 2-D and 3-D scenarios (i.e., a roadside park and the courtyard of an office building in Peking University), respectively, from February 11, 2017 to July 1, 2017, for more than 100 days to collect sufficient data [25].

In the dataset, each *.txt* file includes one complete measurement over a day in one typical scenario. In each *.txt* file, each sample has four parameters, 3-D coordinates (x, y, z) and an AQI value. Each value represents the measured AQI, while its coordinates in the matrix reflect the position in different scenarios. In the 2-D scenario, we assume $z = 0$, while measuring at an interval of 5 m in x and y directions. In the 3-D scenario, every row presents fixed position in xy plane, while every column represents the height at an interval of 5 m in z direction.

C. Data Reliability

To verify that there is no measurement error, we show the results of the relationship between our collected data and the

[1]Dataset can be found online. [Online]. Available: https://github.com/YyzHarry/AQI_Dataset
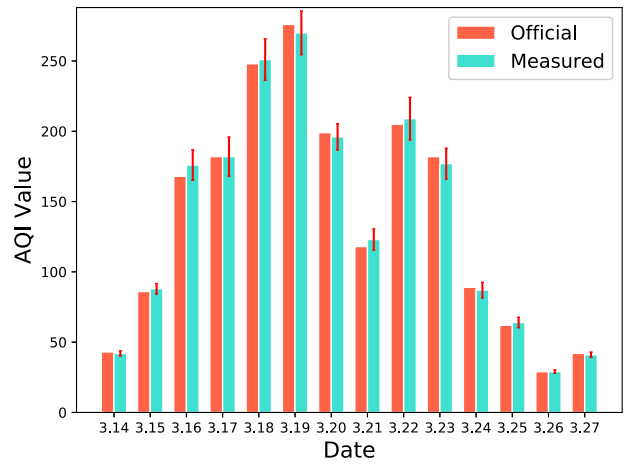

Fig. 3.   AQI value comparison between official data and data we collected, for 14 days in March 2017.

official data (i.e., Haidian station [22]), in Fig. 3. Note that the official data is limited and only for the 2-D space, while our system is mobile and suitable for the 3-D space profiling. We select 14 consecutive days for about 60 instances of monitoring from March 14, 2017 to March 27, 2017, to verify the reliability of our measurement. We use the two-tailed hypothesis test [26]: $\mathcal{H}_0 : \mu_1 = \mu_2$ versus $\mathcal{H}_1 : \mu_1 \neq \mu_2$, where μ_1 denotes our average measured data for all days and μ_2 is the average for the official ones. The test result, $P = 0.9999 \gg 0.05$, indicates that there is no significant difference between the two values, which confirms the reliability of our measurements.

D. Selection of Model Parameters

According to the previous AQI monitoring results for coarse-grained scenarios [17], AQI is related to wind (including speed and direction), temperature, humidity, altitude, and spatial locations. But for fine-grained scenarios, correlations between AQI and these spatial parameters need to be reconsidered, due to the heterogenous diffusion in both vertical and horizontal directions in a small-scale area. In this test, all these potential parameters are measured by our ARMS with different sensors. To evaluate the real correlation between these parameters, we adopt the spatial regression according to [27],

TABLE I
RESULT OF THE HYPOTHESIS TEST

Tested Parameter	P_value
Wind	7.5693×10^{-5} ($\ll 0.05$)
Location	2.0981×10^{-5} ($\ll 0.05$)
Temperature	0.9070 ($\gg 0.05$)
Humidity	0.6996 ($\gg 0.05$)

and test the coefficient for each parameter. Mathematically, the spatio-temporal model is given as

$$C(s_i) = z(s_i)\boldsymbol{\beta}^T + \varepsilon(s_i) \tag{1}$$

where $C(s_i)$ is the particle concentration at position s_i, $z(s_i) = (z_1(s_i), \ldots, z_n(s_i))$ denotes the vector of n parameters at s_i, and $\boldsymbol{\beta} = (\beta_1, \ldots, \beta_n)$ is the coefficient vector. $\varepsilon(s_i) \sim N(0, \sigma^2)$ is the Gaussian white-noise process.

Based on our data, we use the least square regression and implement a hypothesis test for each coefficient β_j, as $\mathcal{H}_0 : \beta_j = 0$. The results in Table I indicate that wind and location are highly related to AQI distribution, whereas temperature and humidity are not.

III. FINE-GRAINED AQI DISTRIBUTION MODEL

In this section, we provide a prediction model considering both physical particle dispersion and NN structure. We first introduce the physical dispersion model for the fine-grained scenario. Then, we provide a brief introduction of NN we adopt in modeling, which can adapt to complicated cases, such as the nonlinearity introduced by extreme weather. Finally, we embed the dispersion model in NN to design our model.

A. Physical Particle Dispersion Model

We first address the physical particle dispersion model for fine-grained scenarios. Specifically, we ignore the influence of temperature and humidity according to discussion in Section II-D, and select the Gaussian plume model (GPM) in the particle movement theory [28], to describe the particle's dispersion. GPM is widely used to describe particles' physical motion [16], [29], and its robustness has been proved in a small scale system [30]. GPM is expressed as

$$C(x, y, z) = \frac{Q}{2\pi \sigma_y \sigma_z u} \exp\left(-\frac{(z-H)^2}{2\sigma_z^2}\right) \exp\left(-\frac{y^2}{2\sigma_y^2}\right) \tag{2}$$

where Q is the point source strength, u is the average wind speed, and H denotes the height of source.

To adopt GPM into the fine-grained scenario, the GPM is revised as

$$
\begin{aligned}
C(\vec{x}, u) &= \int_{-\frac{L}{2}}^{\frac{L}{2}} \frac{\lambda}{2\pi \sigma_y \sigma_z u} \exp\left(-\frac{(z-H)^2}{2\sigma_z^2} - \frac{y^2}{2\sigma_y^2}\right) dy \\
&= \frac{\lambda \exp\left(-\frac{(z-H)^2}{2\sigma_z^2}\right)}{2\pi \sigma_z u} \int_{-\frac{L}{2\sigma_y}}^{\frac{L}{2\sigma_y}} \exp\left(-\frac{\gamma^2}{2}\right) d\gamma \\
&= \frac{\lambda}{\sqrt{2\pi}\sigma_z u} \exp\left(-\frac{(z-H)^2}{2\sigma_z^2}\right) \left[1 - 2Q\left(\frac{L}{2\sigma_y}\right)\right] \tag{3}
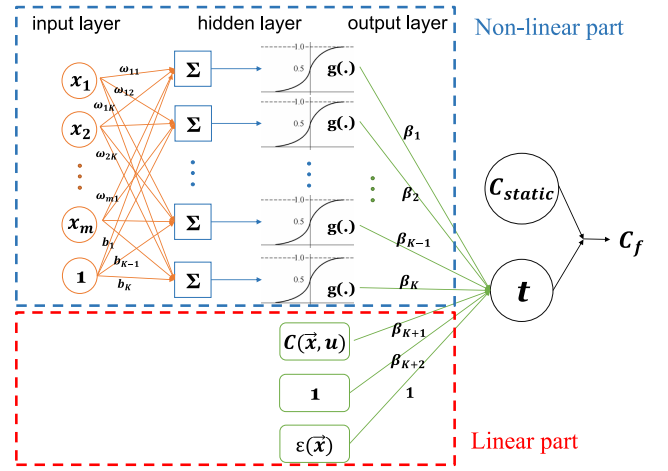\end{aligned}
$$

Fig. 4. Model structure of GPM-NN.

where $C(\vec{x}, u)$ is the AQI value at location $\vec{x}$, u is the real wind speed at different locations in the entire space, and H denotes a variable that reflects the influence of wind direction, which presents severely polluted areas along z-axis. Pollution mainly derives as a line source aligned the y-axis, and L denotes the length of polluted source and λ denotes the particle density at the source. σ_y and σ_z are diffusion parameters in y and z directions, and are both empirically given. The dispersion model in (3) can reflect physical characteristics, but can hardly deal with unpredictable complicated changes, such as the nonlinearity introduced by extreme weather.

B. Neural Network Model

The NN model, especially multilayer perceptron, has been wildly adopted to do estimation for air quality [18]–[21]. They usually train models by using a huge amount of data to achieve decent performance. All possible influential factors are involved as the NN input variables for network training. Other types of NN [31], [32] are proposed for better classification with more complex structures. As it has been proved that a three-layer NN can compute any arbitrary function [33]–[35], NN is able to present the complicated changes in fine-grained scenario. However, without considering the physical characteristics of AQI, the NN model may overfit and perform worse on the test data than on the training data [18].

C. GPM-NN Model

In order to utilize the advantages of both GPM and NN, we embed the revised GPM in NN, and put forward GPM-NN model.

1) Model Description: As shown in Fig. 4, the model structure contains a linear part (the physical dispersion model) and a nonlinear part (the NN structure) for fine-grained AQI distribution, respectively. Let N be the total number of data collected by ARMS, which is represented by a pair (X_j, t_j), where $X_j = [x_1 \ x_2 \ \ldots \ x_m]^\mathrm{T}$ is the jth sample with a dimensionality of m variables and t_j is the measured AQI value.

1) In the nonlinear NN part, let K denote the total number of neurons in the hidden layer. The weights for these

neurons are denoted by $W = [W_1 \; W_2 \; \cdots \; W_K]$, where $W_i = [\omega_{i1} \; \omega_{i2} \; \cdots \; \omega_{im}]$ is the m-dimensional weight vector containing the weights between the components of input vectors and the ith neuron in the hidden layer. $b = [b_1 \; b_2 \; \cdots \; b_K]$ is the bias term of the ith neuron. The nonlinear part with K neurons in the hidden layer will have $\beta = [\beta_1 \; \beta_2 \; \cdots \; \beta_K]$ as weights for output layer and $g(\cdot)$ is the activation function.

2) In the linear part, we use $C(\vec{x}, u)$, a constant value and a Gaussian process as inputs, to reflect the influence of the physical model. The regression weights are correspondingly determined as β_{K+1}, β_{K+2}, and 1.

Thus, the mathematical expression of the proposed model can be written as

$$
t(\vec{x}, u) = \sum_{i=1}^{K} \beta_i g(W_i X_j + b_i) + \beta_{K+1} C(\vec{x}, u) \\
+ \beta_{K+2} + \varepsilon(\vec{x}), \quad j = 1, 2, \ldots, N \quad (4)
$$

where $t(\vec{x}, u)$ is the estimated value of t_j and it represents the model's output. $C(\vec{x}, u)$ is the output of the dispersion model in (3) and β_i are regression coefficients. $\varepsilon(\vec{x}) \sim N(0, \sigma^2)$ is the measurement error defined by a Gaussian white-noise process. Since there is a risk that the NN part will overfit and perform worse on the test data than training data, the estimated AQI value is expressed as

$$
C_f(\vec{x}, u) = C_{\text{static}} + t(\vec{x}, u) \quad (5)
$$

where C_{static} is the average value of our measured AQI in a day, which is an invariant to quantify basic distribution characteristics.

2) Parameter Estimation: As shown in (4), GPM-NN has $(K + 3)$ parameters, $H, \beta_1, \beta_2, \ldots, \beta_{K+2}$, which need to be estimated based on data collected by ARMS. Fifty days' data are used for training the nonlinear part of GPM-NN. We use the least square regression to estimate the parameters. Let $\mathcal{S}$ denote the residual error as

$$
\mathcal{S} = \sum_{i=1}^{N} \left\| \hat{C}_f(\vec{x}_i, u_i) - \beta_{K+2} - \beta_{K+1} C(\vec{x}, u) - \sum_{j=1}^{K} \beta_j g_j \right\|^2 \quad (6)
$$

where i denotes the measuring sample of the ith observation point, and $g_j = g(W_j X_i + b_j)$.

Proposition 1: Equation (6) has a unique minimum point for estimated parameters $\beta_1, \beta_2, \ldots, \beta_{K+2}$ and H, when $\sigma_z^2 > \max\{2z_i^2, 2H_0^2\}$.

Proof: See Appendix. ∎

To find the minimum point of the residual error function $\mathcal{S}(H, \beta_1, \ldots, \beta_{K+2})$, we use the Newton method [36] to solve the following equations whose analytical solution does not exist, as:

$$
\begin{cases}
\dfrac{\partial \mathcal{S}}{\partial H} = 0 \\
\dfrac{\partial \mathcal{S}}{\partial \beta_j} = 0, \quad j = 1, 2, \ldots, K + 2.
\end{cases} \quad (7)
$$

When the estimation value of H (denoted as H^*) is determined, $C(\vec{x}, u)$ is correspondingly determined. Denote

$$
J = \begin{bmatrix}
g(W_1 X_1 + b_1) & \cdots & g(W_K X_1 + b_K) & C(\vec{x}_1, u_1) & 1 \\
g(W_1 X_2 + b_1) & \cdots & g(W_K X_2 + b_K) & C(\vec{x}_2, u_2) & 1 \\
\vdots & \ddots & \vdots & \vdots & \vdots \\
g(W_1 X_N + b_1) & \cdots & g(W_K X_N + b_K) & C(\vec{x}_N, u_N) & 1
\end{bmatrix}_{N \times (K+2)}
$$

as the model output matrix, and similarly

$$
\beta = \begin{bmatrix}
\beta_1 \\
\beta_2 \\
\vdots \\
\beta_K \\
\beta_{K+1} \\
\beta_{K+2}
\end{bmatrix}_{(K+2) \times 1}
$$

is the vector that needs to be estimated. Hence, the estimated value of N samples can be written as

$$
T = J\beta. \quad (8)
$$

Note that J is both row-column full rank matrix, which has a corresponding generalized inverse matrix [37]. As we have proved (6) has a unique minimum point, we then have

$$
\begin{aligned}
\beta &= (J^{\mathrm{T}} J)^{-1} J^{\mathrm{T}} J \beta \\
&= (J^{\mathrm{T}} J)^{-1} J^{\mathrm{T}} T \\
&= J^{\dagger} T
\end{aligned} \quad (9)
$$

where $J^{\dagger} = (J^{\mathrm{T}} J)^{-1} J^{\mathrm{T}}$ is known as the Moore–Penrose pseudo inverse of J. This equation is the least squares solution for an over-determined linear system and is proved to have the unique minimum solution [38]. Thus, this equation is equal to the multivariate equation in (7), by which we can find the minimum value point of $\mathcal{S}$.

3) Performance Evaluation: To determine the initial value of the weights W and biases b for the hidden layer, we use the training data to do preprocessing and acquire the optimal values. Hence, the model can be completely determined for describing the AQI distribution in fine-grained scenarios.

For evaluating the performance of GPM-NN, we use average estimation accuracy (AEA) as the merit, expressed as

$$
\overline{\text{AEA}} = \frac{1}{n} \sum_{i=1}^{n} \left(1 - \frac{\left| \hat{C}_f(i) - C_f(i) \right|}{C_f(i)} \right) \quad (10)
$$

where n denotes the total locations in the scenario, $\hat{C}_f(i)$ denotes the estimation AQI value in the ith location, and $C_f(i)$ denotes the real measured value. In Sections V and VI, we compare the accuracy of AQI map constructed by our GPM-NN and other existing models.

IV. ADAPTIVE AQI MONITORING ALGORITHM

In this section, we provide the adaptive monitoring algorithm of ARMS. Intuitively, a larger number of measurement locations introduce a higher accuracy of the AQI map. However, based on the physical characteristic of particle dispersion in GPM-NN, we can build a sufficiently accurate
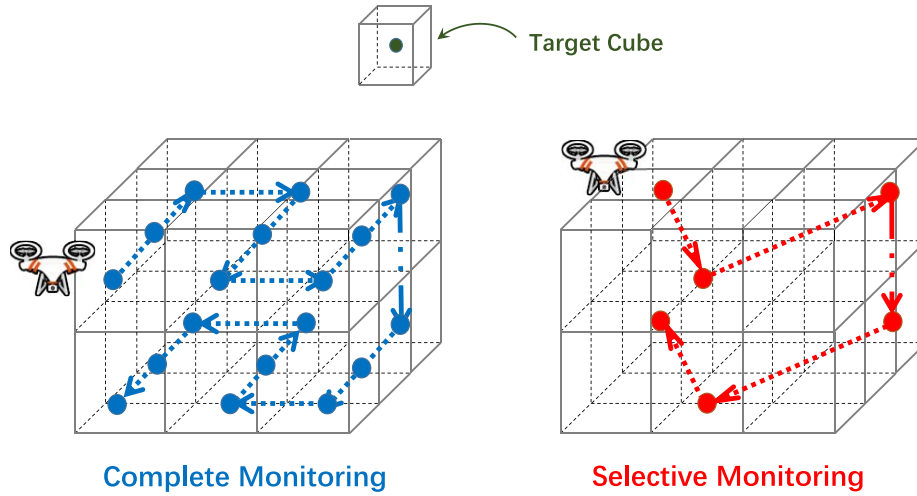
Fig. 5. Example of the adaptive monitoring algorithm, i.e., complete and selective monitoring.

AQI map by regularly measuring only a few locations. This process can effectively save the energy, and thus improve the efficiency of the system. Specifically, an AQI monitoring is decomposed into two steps—*complete monitoring* and *selective monitoring*—for efficiency and accuracy, as shown in Fig. 5. We first trigger *complete monitoring* everyday for one time, to establish a baseline distribution. Then ARMS periodically (e.g., every one hour) measures only a small set of observation points, which are acquired by analyzing the characteristic of the established AQI map. This process, named as *selective monitoring*, is based on GPM-NN to update the real-time AQI map. By accumulating current measurements with the previous map, a new AQI map is generated timely. Every time when selective monitoring is done, ARMS compares the newly measured results and the most recent measurement. If there is a large discrepancy between them, which indicates that the AQI experiences severe environmental changes, we would again trigger the complete monitoring to rebuild the baseline distribution. Thus, ARMS can effectively reduce the measurement effort as well as cope with the unpredictable spatio-temporal variations in the AQI values.

A. Complete Monitoring

The *complete monitoring* is designed to obtain a baseline characteristic of the AQI distribution in a fine-grained area and is triggered at a day interval.

The entire space can be divided into a set of $5 \text{ m} \times 5 \text{ m} \times 5 \text{ m}$ cubes. In the complete monitoring process, ARMS measures all cubes continuously and builds a baseline AQI map using GPM-NN. The process is of high dissipation, and thus is triggered over a long observation period.

B. Selective Monitoring

To reflect changes of the AQI distribution in a small-scale space over time (e.g., between each hour in a day) [11], ARMS uses the *selective monitoring* to capture such dynamics. The selective monitoring makes use of previous AQI map, by

analyzing the physical characteristics of it, to reduce the monitoring overhead in the next survey and maintain the real-time AQI map accordingly.

In the selective monitoring process, ARMS measures AQI value of only a small set of selected cubes and generates AQI map over the entire fine-grained area. To deal with the inherent tradeoff between measurement consumption and accuracy, we put forward an important index called the partial derivative threshold (PDT), to guide system selecting specific cubes. PDT is defined as

$$\text{PDT}_i = \frac{\left|\frac{\partial C_f}{\partial x_i}\right| - \left|\frac{\partial C_f}{\partial x_i}\right|_{\min}}{\left|\frac{\partial C_f}{\partial x_i}\right|_{\max} - \left|\frac{\partial C_f}{\partial x_i}\right|_{\min}} \quad (11)$$

where x_i denotes the ith variable in GPM-NN ($i = 1, 2, \ldots, m$), and $C_f = C_f(\vec{x}, u)$ denotes the entire distribution in a small-scale area. $|\partial C_f/\partial x_i|_{\min}$ and $|\partial C_f/\partial x_i|_{\max}$ denote the minimum and the maximum value of the partial derivative for parameter x_i, respectively. Note that $\partial C_f/\partial x_i$ describes the upper bound of dynamic change degrees we can tolerate, expressed as

$$\frac{\partial C_f}{\partial x_i} = \text{PDT}_i \cdot \left(\left|\frac{\partial C_f}{\partial x_i}\right|_{\max} - \left|\frac{\partial C_f}{\partial x_i}\right|_{\min}\right) + \left|\frac{\partial C_f}{\partial x_i}\right|_{\min}$$
$$0 \leq \text{PDT}_i \leq 1. \quad (12)$$

For each parameter, there is one corresponding PDT. In general, PDT reflects the threshold for dynamic change degrees in a fine-grained area. Area that has large change rate of model's parameters would have a larger PDT value, indicating more drastic changes. When given a specific PDT, any cube whose $\partial C_f/\partial x_i$ is above threshold of (12) will be moved into a set $\mathcal{M}$. Moreover, when PDT_i is too small (less than a small const δ), the corresponding ith cube will also be added into $\mathcal{M}$. Mathematically, set $\mathcal{M}$ is given as

$$\mathcal{M} = \{i \mid \text{PDT}_i \geq \text{PDT}\} \cup \{i \mid \text{PDT}_i \leq \delta\}. \quad (13)$$

Remark 1: Elements in $\mathcal{M}$ can be the severe changing areas in a small-scale space (e.g., a tuyere or abnormal building architecture), or typically the lowest or the highest value that

can reflect basic features of the distribution. These elements are sufficient to depict the entire AQI map, and hence are needed to be measured between two measurements. Thus, by only measuring cubes in $\mathcal{M}$, ARMS can generate a real-time AQI map implemented by GPM-NN, while greatly reducing the measurement overhead.

In general, PDT is adjusted manually for different scenarios. When PDT is low, the threshold for abnormal cubes declines, indicating the measuring cubes will increase and the estimation accuracy is relatively high. However, it can cause great battery consumption. On the other hand, as PDT is high, the measuring cubes will decrease. This can cause a decline in accuracy, but can highly reduce consumption. In summary, the tradeoff between accuracy and consumption should be studied to acquire a better performance of whole system.

C. Trajectory Optimization

When target cubes in set $\mathcal{M}$ are determined, the total network can be modeled as a 3-D graph $G = (V, E)$ with a number of $|V|$ target cubes. Hence, finding the minimum trajectory over these cubes is equal to find the shortest hamiltonian cycle in a 3-D graph. This problem is known as the traveling salesman problem (TSP), which is NP-hard [39].

To solve TSP in this case, we propose a greedy algorithm to find the suboptimal trajectory. In the fine-grained scenario, ARMS has power consumption and can monitor no more than n cubes over one measurement. To find the corresponding trajectory, we focus on how to determine the next measuring cube based on current location of ARMS. Let $\mathbb{Z} = \{O_0, O_1, \ldots, O_{|V|-1}\}$ be the set of coverage cubes, with O_i denotes every observation cube. The aim is to acquire as many target cubes as possible over the trajectory for higher AQI estimation accuracy. Considering the significant physical characteristic of PDT above, our greedy solution can be formulated as: maximize the next cube's PDT, as well as minimize the traveling cost from current location to next cube. Hence, finding the optimal trajectory in this case is equal to an iteration of solving the following optimization problem, expressed as:

$$i^* = \arg\max_i \left| \frac{\text{PDT}_i}{\text{cost}(i)} \right|$$
$$\text{s.t.} \quad O_i \in \mathcal{M}$$
$$O_i \cap \bigcup \{O_0, O_1, \ldots, O_{i-1}\} = \varnothing \quad (14)$$

where $\text{cost}(i)$ is the consumption for the UAV to traverse from the $(i-1)$th cube to the ith cube, and PDT_i is acquired by analyzing the characteristic of latest AQI map.

For every current location i, the selection of next target cube follows (14). Note that there are limited target cubes in $\mathcal{M}$, which are also determined by (12), hence the objective function aims to generate trajectory point-by-point. Thus, using the solution of (14), the greedy algorithm can effectively select key cubes and generate the suboptimal trajectory for ARMS in different scenarios, respectively.

For analyzing the complexity of our algorithm, there are V target cubes in total that need to be added from $\mathcal{M}$. When current location of ARMS is at the ith cube, it needs to

---

Algorithm 1: Operation of Monitoring Algorithm

/* **Complete Monitoring:** triggered between days */
for $i = 1$ *to sum*($Cube$) **do**
    measure the AQI value of $Cube_i$ and record;
    move to the next cube;
end
generate baseline 3D AQI map $\mathbb{B}$;

/* **Selective Monitoring:** triggered between hours */
for $i = 1$ *to sum*($Cube$) **do**
    calculate PDT_{cubei};
    if $PDT_{cubei} \geq PDT$ $||$ $PDT_{cubei} \leq \delta$ **then**
       add $Cube_i$ to $\mathcal{M}$;
    end
end
generate min trajectory $\mathbb{D}$ of $\mathcal{M}$;
forall $p_i \in \mathbb{D}$ **do**
    measure the AQI value of $Cube_i$ and record;
end
update the realtime AQI map $\mathbb{M}$ based on previous $\mathbb{B}$ and $\mathbb{D}$;
if $\mathbb{M}$ *deviates* $\mathbb{B}$ *by a large* σ **then**
    enter the complete monitoring period;
end

---

compare another $|V - i|$ edges in G to determine the next measuring cube. Note that every target cube contains m parameters ($m = 4$ in our model), and $O(V) = O(n)$. Thus, the total operation time is $O(m \sum_{i=1}^{V-1} |V - i|) = O(n^2)$.

Algorithm 1 describes the whole process of the monitoring algorithm. Complete monitoring is triggered between days and selective monitoring is triggered between hours. When the monitoring area experiences severe environmental changes such as the gale, ARMS compares the result of map built by selective monitoring and the map built last time. If there is a large deviation σ between them, ARMS would again trigger the complete monitoring to rebuild the baseline distribution.

V. APPLICATION SCENARIO I: PERFORMANCE ANALYSIS IN HORIZONTAL OPEN SPACE

In this section, we implement the adaptive monitoring algorithm in a typical 2-D scenario, namely the horizontal open space. We present performance analysis of GPM-NN and adaptive monitoring algorithm in this typical scenario, respectively.

A. Scenario Description

When the 3-D space has a limited range in height, ARMS needs to cover target cubes nearly in the same horizontal plane. Two distant cubes at the same height may have a low correlation, as the wind may create different concentration of pollutants in a horizontal plane. This scenario is commonly considered as a typical 2-D scenario and often with a horizontal-open space (e.g., a roadside park), as shown in Fig. 6.
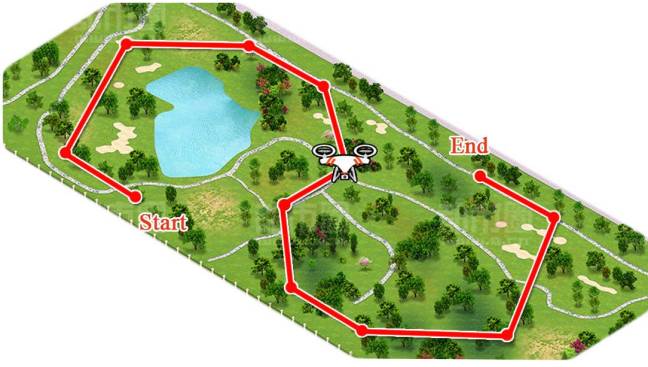
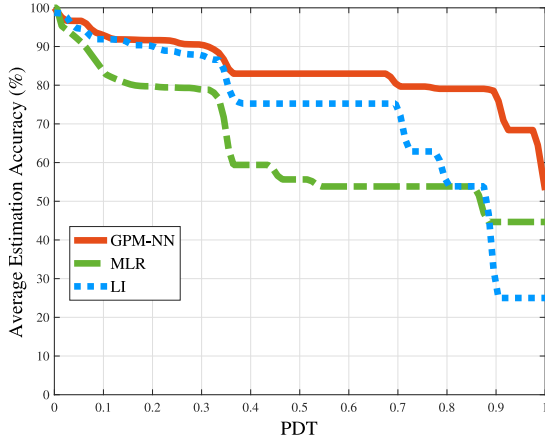Fig. 6. Typical application scenario of ARMS in 2-D space (a roadside park).

Fig. 8. Impact of the number of neurons in the nonlinear part, in 2-D scenario.

Fig. 7. Comparison of estimation accuracy between GPM-NN, MLR, and LI, in 2-D scenario.

B. Performance Analysis

In this section, we first compare the accuracy of GPM-NN with other existing models by the experimental result in Fig. 7. Then, Fig. 8 illustrates the influence by different numbers of neurons in the hidden layer. To study GPM-NN's performance when AQI varies, in Fig. 9, we show the relationship between different AQI values and corresponding estimation accuracy. In Fig. 10, we present the performance of our monitoring algorithm versus other selection algorithms. Finally, Fig. 11 shows the tradeoff between system battery consumptions and estimation accuracy via different PDTs.

1) Model Accuracy: In Fig. 7, we compare three prediction models, our regression model GPM-NN, linear interpolation (LI) [40], and classical multivariable linear regression (MLR) [27], respectively, versus different values of PDT. LI uses interpolation to estimate the AQI value of undetected cubes by other measured cubes, while MLR uses multiple parameters (e.g., wind, humidity, temperature, etc.) of measured cubes to do regression and estimation.

In the horizontal open space scenario, we can find that GPM-NN achieves the highest accuracy. In each curve, we can see that the AEA decreases as the PDT value increases. As discussed in Section IV-B, when PDT has a higher threshold, target cubes in set $\mathcal{M}$ decline, i.e., the total cubes measured by ARMS become fewer. Thus, the estimation
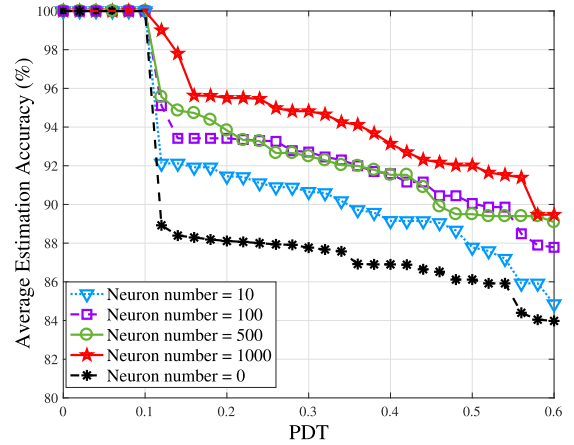
accuracy correspondingly drops. When PDT = 0.1, GPM-NN performs the best among three models, which proves the robust and precision of our model. Moreover, as PDT increases (e.g., PDT = 0.75), GPM-NN still maintains a high accuracy (almost 80%), while others experience a rapid decrease. This implies that our model is suitable for adaptive energy saving monitoring in a fine-grained area.

2) Effects of Neuron Numbers: As we adopt the NN structure to introduce the nonlinear part for our GPM-NN model, the number of neurons in the hidden layer can have great impacts on estimation results. In Fig. 8, we plot the estimation accuracy of different number of neurons in GPM-NN via PDT, to study their influence.

From Fig. 8, when PDT < 0.1, the monitoring contains all cubes. When the number of neurons is 0, our model is equal to the physical model in (3) with regression, which only contains the linear part. By comparing this curve with others, we can find out that the number of neurons = 0 is worse than the number of neurons ≠ 0. By adding the nonlinear part (NN structure), GPM-NN performs better with higher accuracy. Moreover, the curve with fewer number of neurons (e.g., the number of neurons = 10) performs worse than with more neurons (e.g., the number of neurons = 500). In this scenario, we can find that the number of neurons = 1000 can achieve the highest estimation accuracy. We ignore the situation where the number of neurons > 1000, as too many neurons in the hidden layer can cause overfitting.

3) Effects of Various AQI: In Fig. 9, we plot the estimation accuracy of GPM-NN with different AQI values (i.e., AQI ≤ 50, 50 ≤ AQI ≤ 200, and AQI ≥ 200 [22]), via different PDTs. From the curves, we can find that in 2-D scenario, GPM-NN performs the best when AQI ≥ 200. As 50 ≤ AQI ≤ 200, GPM-NN also maintains high accuracy, while relatively worse when AQI is low. This indicates that our model is better predicting in moderately and highly polluted days, which has great instructing significance in forecasting severe pollution as well as prevention. This characteristic is also suitable for the adaptive monitoring algorithm when AQI is high. Note that even GPM-NN performs not so good when AQI is low, it still outperforms other models.
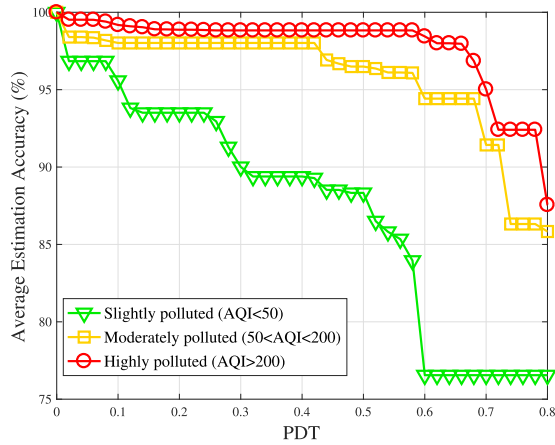
Fig. 9. Performance of GPM-NN with different AQI values, in 2-D scenario.
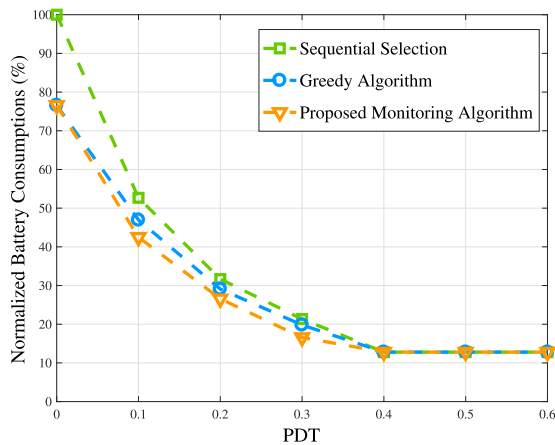

Fig. 11.   Tradeoff between system battery consumption and estimation accuracy, in 2-D scenario.

Fig. 10. Comparison of the adaptive monitoring algorithm, greedy algorithm, and sequential selection, in 2-D scenario.

4) Performance of Adaptive Monitoring Algorithm: In this part, we compare the results of the proposed monitoring algorithm for trajectory planning, versus other algorithms such as greedy algorithm and sequential selection, by plotting their battery consumptions over one measurement in Fig. 10. The greedy algorithm aims to select the nearest target cube in $\mathcal{M}$ to generate the trajectory [9], while sequential selection is done by selecting cubes from the bottom (or left) to the top (or right) in order [11].

In the typical horizontal open space, we plot the normalized battery consumption achieved by three algorithms in Fig. 10, via different PDTs. The normalized consumption is the cost percentage achieved by each monitoring method of one total battery charge (i.e., 15 min). As PDT increases, the consumption would correspondingly decrease, as the target cubes in $\mathcal{M}$ would be fewer. By comparing three curves, we can see that sequential selection is the most consuming method. Our monitoring algorithm performs the best and is better than the normal greedy algorithm, while $0.1 \leq \text{PDT} \leq 0.4$. After PDT reaches 0.4, the consumption of three methods becomes equal, since the target cubes in $\mathcal{M}$ now is so few that there is no difference in using these algorithm. Hence, the adaptive monitoring
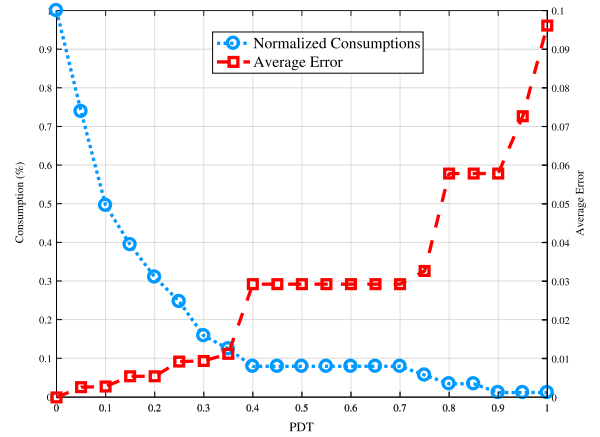
algorithm can relatively reduce the power consumption for monitoring AQI in the 2-D scenario.

5) Tradeoff Between Consumption and Accuracy: In Fig. 11, we illustrate the tradeoff between the battery consumption and estimation accuracy. To better illustrate the tradeoff, we use *average error* as a merit, expressed as

$$\overline{\text{ERR}} = \frac{1}{n} \sum_{i=1}^{n} \left(\frac{\hat{C}_f(i) - C_f(i)}{C_f(i)} \right)^2 \qquad (15)$$

where n, $\hat{C}_f(i)$, and $C_f(i)$ are the same in (10). We plot the curves of system's power consumption and average estimation error versus PDT.

Fig. 11 illustrates the relationship between the accuracy and the battery consumption. Intuitively, a larger PDT introduces less power consumption, which proves that with a higher PDT, consumption declines as the number of measured cubes decreases. Moreover, when $\text{PDT} \geq 0.4$, the total consumption of the whole system can be reduced by 90%. The rapid decline of consumption is also related to the high redundancy of data in the typical 2-D space as the roadside park. On the other hand, the average error of ARMS increases as PDT becomes larger, which confirms the existence of the tradeoff between power consumption and estimation accuracy. Under this circumstance, choose $\text{PDT} = 0.41$ can achieve a relatively high predicting accuracy (over 80%) while greatly reduce the battery consumption of the system.

VI. Application Scenario II: Performance Analysis in Vertical Enclosed Space

In this section, we implement the adaptive monitoring algorithm in a typical 3-D scenario, vertical enclosed space. We then present performance analysis of the GPM-NN and the adaptive monitoring algorithm in this typical scenario, respectively.

A. Scenario Description

In the typical 3-D scenario, the 3-D space has target cubes in various heights. In this type of scenario, the planar area is relatively limited (e.g., the courtyard inside a high-rise building).
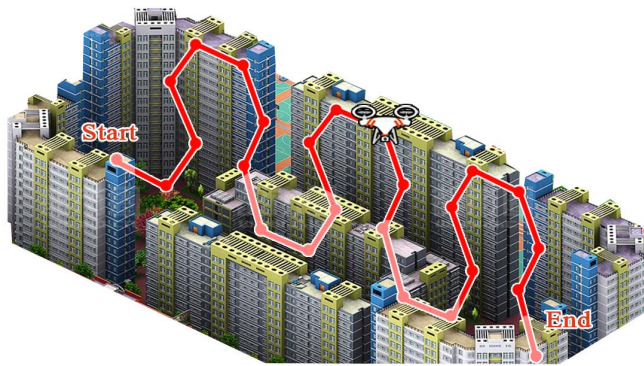
Fig. 12. Typical application scenario of ARMS in 3-D space (courtyard inside a high-rise building).

Fig. 13. Comparison of estimation accuracy between GPM-NN, MLR, and LI, in 3-D scenario.

As shown in Fig. 12, in such a vertical enclosed space, there is no significant difference on AQI values between two horizontally neighboring cubes, but the wind may create a discrepancy of the pollutant concentration on two cubes at different heights. Hence, the benefit of selecting more cubes vertically outweigh the cost of traversing between distant cubes at the same heights.

B. Performance Analysis

In this section, we present performance analysis of ARMS in different aspects, as in Section V-B, for typical 3-D scenario.

1) Model Accuracy: In Fig. 13, we compare three prediction models. In the vertical enclosed space scenario, GPM-NN still maintains the highest accuracy among three models via different PDTs. Compared to 2-D scenario, LI decreases rapidly as PDT increases, which indicates the heterogenous in 3-D AQI distribution. Moreover, when PDT = 0.8, GPM-NN would experience a violent decline. This phenomenon is caused by the inherent characteristic of PDT. When PDT is high, the corresponding number of target cubes in $\mathcal{M}$ becomes so few that the predicting accuracy can significantly drop, even if only one point unmeasured (e.g., ten cubes with PDT = 0.75 and nine cubes with PDT = 0.8). This result can provide the basis for choosing the suitable PDT value.

In conclusion, GPM-NN performs better in both 2-D and 3-D fine-grained scenarios, with high estimation accuracy even if measuring cubes are few.

2) Effects of Neuron Numbers: In Fig. 14, we study the effects of the number of neurons in a typical 3-D scenario. When PDT < 0.1, the result is the same as in the 2-D scenario, that each curve performs the best. As PDT increases, the curve with the number of neurons = 0 declines most rapidly like that in Fig. 8. Also, the curve with fewer number of neurons (e.g., the number of neurons = 10) performs worse than with more neurons (e.g., the number of neurons = 100/1000) as well. In this scenario, we can find that the number of neurons = 500 can achieve the highest estimation accuracy, which is different from the result in the 2-D scenario.

In conclusion, our GPM-NN model (with combination of linear and nonlinear part) is robust and better than that with
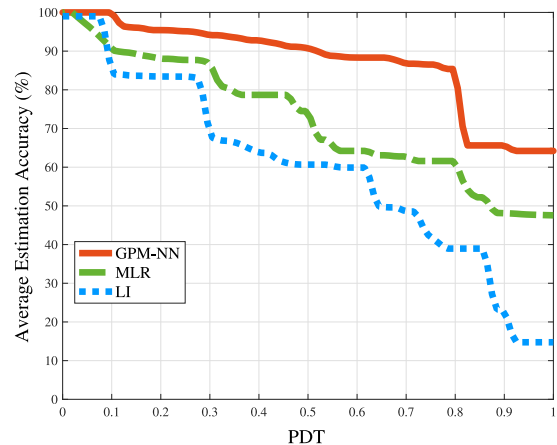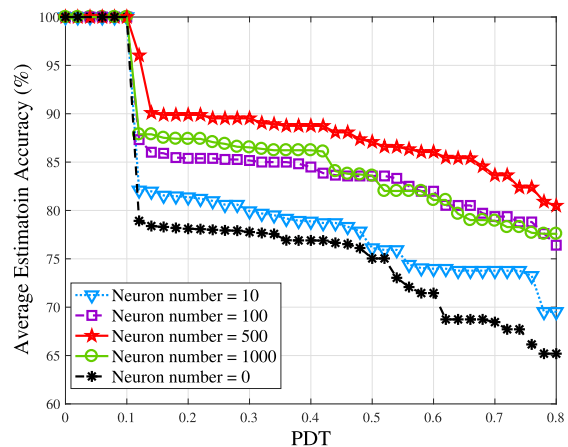

Fig. 14. Impact of the number of neurons in the nonlinear part, in 3-D scenario.
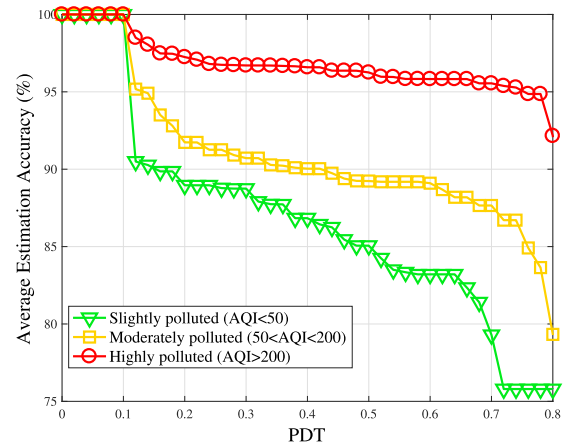

Fig. 15. Performance of GPM-NN with different AQI values, in 3-D scenario.

only linear part. Moreover, the number of neurons in the hidden layer can effectively influence the model's performance, and the optimal value is different in various scenarios.

3) Effects of Various AQI: In Fig. 15, we again plot the estimation accuracy of GPM-NN with different AQI values in the 3-D scenario. From the curves, we can find that GPM-NN
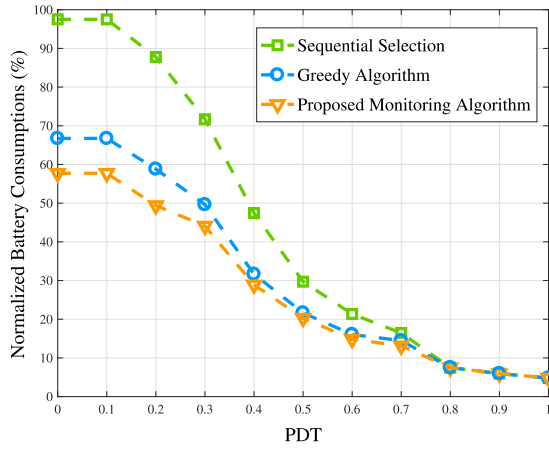
Fig. 16. Comparison of the adaptive monitoring algorithm, greedy algorithm, and sequential selection, in 3-D scenario.
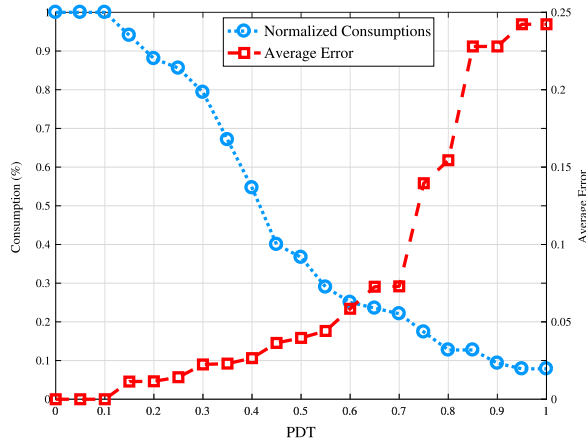

Fig. 17. Tradeoff between system battery consumption and estimation accuracy, in 3-D scenario.

also performs the best when moderately and highly polluted, while relatively worse when AQI is low.

In conclusion, GPM-NN can maintain better estimation accuracy when the AQI value is moderate and high, which is suitable for the operation of our ARMS.

4) Performance of Adaptive Monitoring Algorithm: In the 3-D scenario as vertical enclosed space, Fig. 16 shows the consumption of three algorithms, our monitoring algorithm, greedy algorithm and sequential selection, via different PDTs. From the figure, we can see when PDT is low, sequential selection consumes much more than those of our method and greedy algorithm. This indicates that when scenario becomes 3-D, the cube selection can be more complicated and a suitable selection method can highly reduce the battery consumption. Moreover, adaptive monitoring algorithm also performs the best among three methods, and it is better than the greedy algorithm when PDT ≤ 0.8. As PDT becomes high, the normalized consumption of three algorithms is closer, and becomes equal when PDT ≥ 0.8. Thus, the adaptive monitoring algorithm can effectively save the battery life for monitoring AQI in 3-D scenario.

5) Tradeoff Between Consumption and Accuracy: In Fig. 17, we plot the tradeoff in the 3-D scenario as horizontal

enclosed space. This typical 3-D scenario is more common in real measurement, and hence the result is more instructive. As PDT becomes higher, the average error grows rapidly as consumption can drop fairly. Given the average error, for example, when $\overline{\text{ERR}} = 0.04$ (AEA is about 80%), the corresponding PDT = 0.51, and thus the power consumption can be reduced to as little as 37%. Hence, by choosing suitable PDT value for monitoring, the measuring efforts can greatly scale down.

VII. Conclusion

In this paper, we have designed a UAV sensing system, ARMS, to construct fine-grained AQI maps. A novel fine-grained AQI distribution model GPM-NN has been proposed based on NN and physical model, to help generate a real-time AQI map with data collected by ARMS. To reduce the battery consumptions of ARMS, we have proposed the adaptive monitoring algorithm to efficiently update real-time AQI maps. For the 2-D and 3-D scenarios, we have applied the adaptive monitoring algorithm, respectively. By using the proposed index PDT, the system can well balance the intrinsic tradeoff between the estimation accuracy and power consumption. Experimental results have shown that GPM-NN can achieve a higher accuracy in AQI map construction than other existing models, and the number of neurons in the hidden layer of GPM-NN should also be adjusted in various scenarios to acquire better performance. Moreover, the adaptive monitoring algorithm can generate the trajectory while greatly saving the battery life of the UAV, and ARMS can well balance the tradeoff between accuracy of AQI map and battery consumptions.

Appendix
Proof of Proposition 1

For β_j where $j \in [1, K+2]$, we have

$$\frac{\partial^2 \mathcal{S}}{\partial \beta_j^2} = \begin{cases} 2\sum_{i=1}^{N} g_j^2 > 0, & 1 \leq j \leq K \\ 2\sum_{i=1}^{N} C^2(\vec{x}_i, u_i) > 0, & j = K+1 \\ 2\sum_{i=1}^{N} 1 = 2N > 0, & j = K+2. \end{cases} \quad (16)$$

Hence, $\partial \mathcal{S}/\partial \beta_j$ are all convex functions, with $j \in [1, K+2]$.

As for variable H, the second order partial derivative can be calculated as

$$\frac{\partial^2 \mathcal{S}}{\partial H^2}$$

$$= -2\sum_{i=1}^{N} \beta' \left[-\frac{\beta'}{\sigma_z^6 u_i^2}(z_i - H)^2 \exp\left(-\frac{(z_i - H)^2}{\sigma_z^2}\right) \right.$$

$$- \left(C - \frac{\beta' \exp\left(-\frac{(z_i - H)^2}{2\sigma_z^2}\right)}{u_i \sigma_z}\right) \frac{1}{u_i \sigma_z^3} \exp\left(-\frac{(z_i - H)^2}{2\sigma_z^2}\right)$$

$$\left. + \left(C - \frac{\beta' \exp\left(-\frac{(z_i - H)^2}{2\sigma_z^2}\right)}{u_i \sigma_z}\right) \frac{(z_i - H)^2 \exp\left(-\frac{(z_i - H)^2}{2\sigma_z^2}\right)}{u_i \sigma_z^5} \right]$$

where $C = (\hat{C}_f(\vec{x}_i, u_i) - C_{\text{static}} - \beta_{K+2} - \sum_{j=1}^{K} \beta_j g_j)$ and $\beta' = (\lambda/\sqrt{2\pi})\beta_{K+1}(1 - 2Q(L/2\sigma_y))$. Then we have

$$\frac{\partial^2 \mathcal{S}}{\partial H^2} = 2\sum_{i=1}^{N}\left[\left(\frac{2\beta'^2(z_i - H)^2}{\sigma_z^6 u_i^2} - \frac{\beta'^2}{\sigma_z^4 u_i^2}\right)\exp\left(-\frac{(z_i - H)^2}{\sigma_z^2}\right)\right.$$
$$\left. + C\left(\frac{\beta'}{\sigma_z^3 u_i} - \frac{\beta'(z_i - H)^2}{u_i \sigma_z^5}\right)\exp\left(-\frac{(z_i - H)^2}{2\sigma_z^2}\right)\right].$$

Let $t_i = \exp(-[((z_i - H)^2)/2\sigma_z^2])$, each item of the summation is equivalent to a quadratic function $Q_i(t_i) = a_i t_i^2 + b_i t_i$. Note that $t_i \in (0, 1]$, and $t_i = 0$ is one zero point of $Q_i(t_i)$. To satisfy the proposition that $\partial^2 \mathcal{S}/\partial H^2$ always has positive value, the problem becomes

$$\begin{cases} a_i = \dfrac{2\beta'^2(z_i - H)^2}{u_i^2 \sigma_z^6} - \dfrac{\beta'^2}{u_i^2 \sigma_z^4} < 0 \\ b_i = C\left(\dfrac{\beta'}{u_i \sigma_z^3} - \dfrac{\beta'(z_i - H)^2}{u_i \sigma_z^5}\right) > 0 \end{cases} \quad \forall i \in [1, N]$$

which can be simplified as

$$\begin{cases} \sigma_z^2 > \max_i \; 2(z_i - H)^2 \\ \sigma_z^2 > \max_i \; (z_i - H)^2. \end{cases} \tag{17}$$

We define $H \in [0, H_0]$, where H_0 is the upper bound for a fine-grained measurement. Hence, by choosing appropriate diffusion parameter σ_z as $\sigma_z^2 > \max\{2z_i^2, 2H_0^2\}$, we have

$$\frac{\partial^2 \mathcal{S}}{\partial H^2} = 2\sum_{i=1}^{N} Q_i(t_i)$$
$$= 2\sum_{i=1}^{N}\left(a_i t_i^2 + b_i t_i\right)$$
$$= 2\sum_{i=1}^{N}\left(\frac{b_i^2}{4|a_i|} - |a_i|\left(t_i + \frac{b_i}{2a_i}\right)^2\right) > 0 \quad \forall t_i \in (0, 1].$$

Therefore, $\partial \mathcal{S}/\partial H$ is also a convex function, which indicates that (6) has a minimum as well as a unique value, correspondingly.

REFERENCES

[1] World Health Organization, "7 million premature deaths annually linked to air pollution," *Air Qual. Climate Change*, vol. 22, no. 1, pp. 53–59, Mar. 2014.

[2] Q. Di *et al.*, "Air pollution and mortality in the medicare population," *New England J. Med.*, vol. 376, no. 26, pp. 2513–2522, Jul. 2017.

[3] Y. Li *et al.*, "Prediction of high resolution spatial–temporal air pollutant map from big data sources," in *Proc. Int. Conf. Big Data Comput. Commun.*, Taiyuan, China, Jul. 2015, pp. 273–282.

[4] B. Zou, J. G. Wilson, F. B. Zhan, and Y. N. Zeng, "Air pollution exposure assessment methods utilized in epidemiological studies," *J. Environ. Monitor.*, vol. 11, no. 3, pp. 475–490, Feb. 2009.

[5] Beijing MEMC. (Mar. 2017). *Beijing Municipal Environmental Monitoring Center*. [Online]. Available: http://www.bjmemc.com.cn/

[6] Y. Cheng *et al.*, "AirCloud: A cloud-based air-quality monitoring system for everyone," in *Proc. 12th ACM Conf. Embedded Netw. Sensor Syst.*, Memphis, TN, USA, Nov. 2014, pp. 251–265.

[7] D. Hasenfratz *et al.*, "Deriving high-resolution urban air pollution maps using mobile sensor nodes," *Pervasive Mobile Comput.*, vol. 16, no. 2, pp. 268–285, Jan. 2015.

[8] N. Nikzad *et al.*, "CitiSense: Improving geospatial environmental assessment of air quality using a wireless personal exposure monitoring system," in *Proc. ACM Wireless Health*, San Diego, CA, USA, Oct. 2010, p. 11.

[9] Y. Gao *et al.*, "Mosaic: A low-cost mobile sensing system for urban air quality monitoring," in *Proc. IEEE Int. Conf. Comput. Commun. (INFOCOM)*, San Francisco, CA, USA, Apr. 2016, pp. 1–9.

[10] D. S. Bisht *et al.*, "Tethered balloon-born and ground-based measurements of black carbon and particulate profiles within the lower troposphere during the foggy period in Delhi, India," *Sci. Total Environ.*, vol. 573, no. 1, pp. 894–905. Dec. 2016.

[11] Y. Hu, G. Dai, J. Fan, Y. Wu, and H. Zhang, "BlueAer: A fine-grained urban PM2.5 3D monitoring system using mobile sensing," in *Proc. IEEE Int. Conf. Comput. Commun. (INFOCOM)*, San Francisco, CA, USA, Jul. 2016, pp. 1–9.

[12] T. N. Quang, C. He, L. Morawska, L. D. Knibbs, and M. Falk, "Vertical particle concentration profiles around urban office buildings," *Atmos. Chem. Phys.*, vol. 12, no. 11, pp. 5017–5030, May 2012.

[13] F. M. Rubinoa *et al.*, "Height profile of some air quality markers in the urban atmosphere surrounding a 100 m tower building," *Atmos. Environ.*, vol. 32, no. 20, pp. 3569–3580. Sep. 1998.

[14] C. Borrego *et al.*, "How urban structure can affect city sustainability from an air quality perspective," *Environ. Model. Softw.*, vol. 21, no. 4, pp. 461–467, Apr. 2006.

[15] Y. Zheng, F. Liu, and H.-P. Hsieh, "U-Air: When urban air quality inference meets big data," in *Proc. 19th ACM SIGKDD Int. Conf. Knowl. Disc. Data Min. (KDD)*, Chicago, IL, USA, Aug. 2013, pp. 1436–1444.

[16] H.-X. Xu, G. Li, S.-L. Yang, and X. Xu, "Modeling and simulation of haze process based on Gaussian model," in *Proc. 11th Int. Comput. Conf. Wavelet Actiev Media Technol. Inf. Process. (ICCWAMTIP)*, Chengdu, China, Apr. 2014, pp. 68–74.

[17] M. Cameletti, R. Ignaccolo, and S. Bande, "Comparing spatio-temporal models for particulate matter in Piemonte," *Environmetrics*, vol. 22, no. 8, pp. 985–996. Dec. 2011.

[18] C. Zhao, M. van Heeswijk, and J. Karhunen, "Air quality forecasting using neural networks," in *Proc. IEEE Symp. Series Comput. Intell. (SSCI)*, Athens, Greece, Dec. 2016, pp. 1–7.

[19] M. Cai, Y. Yin, and M. Xie, "Prediction of hourly air pollutant concentrations near urban arterials using artificial neural network approach," *Transp. Res. D Transp. Environ.*, vol. 14, no. 1, pp. 32–41, Jan. 2009.

[20] M. W. Gardner and S. R. Dorling, "Neural network modelling and prediction of hourly NO_x and NO_2 concentrations in urban air in London," *Atmos. Environ.*, vol. 33, no. 5, pp. 709–719, Feb. 1999.

[21] M. M. Dedovic, S. Avdakovic, I. Turkovic, N. Dautbasic, and T. Konjic, "Forecasting PM10 concentrations using neural networks and system for improving air quality," in *Proc. XI Int. Symp. Telecommun. (BIHTEL)*, Sarajevo, Bosnia and Herzegovina, Oct. 2016, pp. 1–6.

[22] Beijing EPB. (Mar. 2017). *Beijing Municipal Environmental Protection Bureau*. [Online]. Available: http://www.bjepb.gov.cn/

[23] Plantower. *Technology Laser PM2.5 Sensor, Air Quality Sensor*. Accessed: Jul. 2017. [Online]. Available: http://www.plantower.com/en/

[24] *Da-Jiang Innovations Science and Technology Co., Ltd. (DJI), Phantom 3 Professional*. Accessed: Jul. 2017. [Online]. Available: https://www.dji.com/cn/phantom-3-pro

[25] Y. Yang *et al.*, "Arms: A fine-grained 3D AQI realtime monitoring system by UAV," in *Proc. IEEE Glob. Commun. Conf. (GLOBECOM)*, Singapore, Dec. 2017, pp. 1–6.

[26] R. V. Hogg and A. T. Craig, *Introduction to Mathematical Statistics*, 5th ed. Upper Saddle River, NJ, USA: Prentice-Hall. 1995.

[27] M. Cameletti, F. Lindgren, D. Simpson, and H. Rue, "Spatio-temporal modeling of particulate matter concentration through the SPDE approach," *Adv. Stat. Anal.*, vol. 97, no. 2, pp. 109–131. Apr. 2013.

[28] D. R. Middleton, "Modelling air pollution transport and deposition," in *Proc. IEE Colloquium Pollution Land Sea Air Overview Eng.*, London, U.K., Oct. 1995, pp. 1–7.

[29] J. M. Stockie, "The mathematics of atmospheric dispersion modeling," *SIAM Review*, vol. 53, no. 2, pp. 349–372, May 2011.

[30] S. Brusca *et al.*, "Theoretical and experimental study of Gaussian plume model in small scale system," *Energy Procedia*, vol. 101, no. 1, pp. 58–65, Nov. 2016.

[31] F. Tang *et al.*, "On removing routing protocol from future wireless networks: A real-time deep learning approach for intelligent traffic control," *IEEE Wireless Commun.*, to be published.

[32] A. Al-Molegi, M. Jabreel, and B. Ghaleb, "STF-RNN: Space time features-based recurrent neural network for predicting people next location," in *Proc. IEEE Symp. Series Comput. Intell. (SSCI)*, Athens, Greece, Dec. 2016, pp. 1–7.

[33] S. M. Carroll and B. W. Dickinson, "Construction of neural nets using the Radon transform," in *Proc. IEEE Int. Joint Conf. Neural Netw.*, Washington, DC, USA, Feb. 1989, pp. 607–611.

[34] G. Cybenko, "Approximation by superpositions of a sigmoidal function," *Math. Control Signals Syst.*, vol. 2, no. 4, pp. 303–314, Dec. 1989.

[35] K.-I. Funahashi, "On the approximate realization of continuous mappings by neural networks," *Neural Netw.*, vol. 2, no. 3, pp. 183–192, Feb. 1989.

[36] D. P. Bertsekas, *Nonlinear Programming*. Belmont, MA, USA: Athena Sci., 1999. pp. 1–60.

[37] R. Penrose, "A generalized inverse for matrices," *Math. Proc. Cambridge Philosoph. Soc.*, vol. 51, no. 3, pp. 406–413, Jul. 1955.

[38] R. MacAusland, "The Moore–Penrose inverse and least squares," in *Math 420: Advanced Topics in Linear Algebra*. Tacoma, WA, USA: Univ. Puget Sound, 2014, pp. 1–10.

[39] D. E. Goldberg and R. Lingle, "Alleles, loci, and the traveling salesman problem," in *Proc. Int. Conf. Genet. Algorithms Appl.*, vol. 154. Hillsdale, NJ, USA, Jul. 1985, pp. 154–159.

[40] C. de Boor, *A Practical Guide to Splines*. New York, NY, USA: Springer-Verlag, 1978.

Kaigui Bian (S'05–M'11) is an Associate Professor with the School of Electronics Engineering and Computer Science, Peking University, Beijing, China. His current research interests include mobile computing, cognitive radio networks, and network security and privacy.

Mr. Bian was a recipient of the Best Paper Award of IEEE ICC 2015 and ICCSE 2017 and the 2014 CCF-Intel Young Faculty Researcher Award.

Lingyang Song (S'03–M'06–SM'12) is a Professor with the School of Electronics Engineering and Computer Science, Peking University, Beijing, China. His current research interests include MIMO, cognitive and cooperative communications, security, and big data.

Mr. Song was a recipient of the IEEE Leonard G. Abraham Prize in 2016 and the IEEE Asia–Pacific Young Researcher Award in 2012. He is currently on the Editorial Board of the IEEE Transactions on Wireless Communications.

Yuzhe Yang (S'17) is currently pursuing the B.S. degree at the School of Electrical Engineering and Computer Science, Peking University, Beijing, China.

His current research interests include wireless networks, mobile sensing and computing, and machine learning.

Zhu Han (S'01–M'04–SM'09–F'14) received the B.S. degree in electronic engineering from Tsinghua University, Beijing, China, in 1997, and the M.S. and Ph.D. degrees in electrical and computer engineering from the University of Maryland at College Park, College Park, MD, USA, in 1999 and 2003, respectively.

From 2000 to 2002, he was an Research and Development Engineer with JDSU, Germantown, MD, USA. From 2003 to 2006, he was a Research Associate with the University of Maryland at College Park. From 2006 to 2008, he was an Assistant Professor with Boise State University, Boise, ID, USA. He is currently a Professor with the Electrical and Computer Engineering Department and the Computer Science Department, University of Houston, Houston, TX, USA. His current research interests include wireless resource allocation and management, wireless communications and networking, game theory, big data analysis, security, and smart grid.

Dr. Han was a recipient of the NSF Career Award in 2010, the Fred W. Ellersick Prize of the IEEE Communication Society in 2011, the EURASIP Best Paper Award for the *Journal on Advances in Signal Processing* in 2015, the IEEE Leonard G. Abraham Prize in the field of communications systems (the Best Paper Award of the IEEE Journal on Selected Areas in Communications) in 2016, and several Best Paper Awards of IEEE conferences. He is currently an IEEE Communications Society Distinguished Lecturer.

Zijie Zheng (S'14) received the B.S. degree in electronic engineering from Peking University, Beijing, China, in 2014, where he is currently pursuing the Ph.D. degree at the School of Electrical Engineering and Computer Science.

His current research interests include game theory in 5G networks, wireless powered networks, mobile social networks, and wireless big data.